Title

Simultaneous measurement of T2 and apparent diffusion coefficient (T2+ADC) in the heart with motion-compensated spin echo diffusion-weighted imaging

Journal

Magnetic Resonance in Medicine, 79(2)

ISSN

0740-3194

Authors

Aliotta, Eric
Moulin, Kévin
Zhang, Zhaohuan
et al.

Publication Date

2018-02-01

DOI

10.1002/mrm.26705

Peer reviewed

FULL PAPER

Magnetic Resonance in Medicine 00:00–00 (2017)

Simultaneous Measurement of T_2 and Apparent Diffusion Coefficient (T_2+ADC) in the Heart With Motion-Compensated Spin Echo Diffusion-Weighted Imaging

Eric Aliotta,[1,2] Kévin Moulin,[1] Zhaohuan Zhang,[1,3] and Daniel B. Ennis[1,2,3]*

Purpose: To evaluate a technique for simultaneous quantitative T_2 and apparent diffusion coefficient (ADC) mapping in the heart (T_2+ADC) using spin echo (SE) diffusion-weighted imaging (DWI).

Theory and Methods: T_2 maps from T_2+ADC were compared with single-echo SE in phantoms and with T_2-prepared (T_2-prep) balanced steady-state free precession (bSSFP) in healthy volunteers. ADC maps from T_2+ADC were compared with conventional DWI in phantoms and in vivo. T_2+ADC was also demonstrated in a patient with acute myocardial infarction (MI).

Results: Phantom T_2 values from T_2+ADC were closer to a single-echo SE reference than T_2-prep bSSFP ($-2.3 \pm 6.0\%$ vs $22.2 \pm 16.3\%$; $P < 0.01$), and ADC values were in excellent agreement with DWI ($0.28 \pm 0.4\%$). In volunteers, myocardial T_2 values from T_2+ADC were significantly shorter than T_2-prep bSSFP (35.8 ± 3.1 vs 46.8 ± 3.8 ms; $P < 0.01$); myocardial ADC was not significantly (N.S.) different between T_2+ADC and conventional motion-compensated DWI (1.39 ± 0.18 vs $1.38 \pm 0.18\,mm^2/ms$; $P =$ N.S.). In the patient, T_2 and ADC were both significantly elevated in the infarct compared with remote myocardium (T_2: 40.4 ± 7.6 vs 56.8 ± 22.0; $P < 0.01$; ADC: 1.47 ± 0.59 vs $1.65 \pm 0.65\,mm^2/ms$; $P < 0.01$).

Conclusion: T_2+ADC generated coregistered, free-breathing T_2 and ADC maps in healthy volunteers and a patient with acute MI with no cost in accuracy, precision, or scan time compared with DWI. **Magn Reson Med 000:000–000, 2017. © 2017 International Society for Magnetic Resonance in Medicine.**

Key words: Cardiac; T_2 Mapping; DWI

INTRODUCTION

Cardiac diffusion-weighted imaging (cDWI) has high potential diagnostic value for quantifying the extent and degree of diffuse and focal myocardial fibrosis (1,2) without the need for a gadolinium-based contrast agent. cDWI measures the self-diffusion of water molecules in soft tissues and can detect fibrosis by increases in the apparent diffusion coefficient (ADC) that accord with the increase in extracellular volume. This can enable myocardial infarction (MI) evaluation for the ~40% of cardiovascular disease patients with impaired renal function in whom the use of gadolinium-based contrast agents is contraindicated (3,4).

Conventional DWI approaches are extremely sensitive to bulk motion, but recent developments in gradient hardware and the emergence of bulk motion-compensated (MOCO) diffusion encoding techniques have enabled robust DWI in the heart (5,6). In this study, we use convex optimized diffusion encoding (CODE) (7) with first- (M_1) and second-order (M_2) motion compensation (CODE-M_1M_2). CODE-M_1M_2 simultaneously imparts insensitivity to bulk motion and improves pulse sequence acquisition efficiency, by minimizing the echo time (TE) for a given b-value. The CODE approach enables higher resolution or higher signal-to-noise (SNR) cardiac MOCO DWI with shorter TEs than other techniques.

Quantitative T_2 mapping is also a valuable tool for myocardial tissue characterization. For example, increases in T_2 can indicate the presence of myocardial edema (8,9), and decreases in T_2 have been observed in iron overload (10), which can occur in thalassemia as well as in hemorrhagic MI (11). The combination of quantitative T_2 maps for detecting edema or iron overload and DWI maps for identifying myocardial fibrosis can potentially be used to differentiate infracts and score the extent and degree of focal and diffuse fibrosis for a variety of pathologies.

Herein, we describe a free-breathing technique that jointly measures cardiac T_2 and ADC (T_2+ADC), thereby generating maps that are perfectly coregistered and acquired at the same cardiac phase. T_2+ADC requires only minor modification to the spin-echo DWI acquisition and does not increase scan time compared to conventional ADC mapping alone. In this study, T_2+ADC was evaluated through Bloch equation simulations, validated with quantitative phantom imaging, and demonstrated in healthy volunteers and in a patient with acute MI.

THEORY

DWI acquisitions typically use a spin-echo (SE) sequence with a single-shot echo planar imaging (EPI) readout wherein several images are acquired at a fixed TE with diffusion weighting along multiple directions. The diffusion

[1]Department of Radiological Sciences, University of California, Los Angeles, California, USA.

[2]Biomedical Physics Interdepartmental Program, University of California, Los Angeles, California, USA.

[3]Department of Bioengineering, University of California, Los Angeles, California, USA.

Grant sponsor: Graduate Program in Bioscience at UCLA; Grant sponsor: Department of Radiological Sciences at UCLA; Grant sponsor: NIH; Grant number: R01HL131975; Grant sponsor: AHA; Grant number: 16PRE27380023.

*Correspondence to: Daniel B. Ennis, Ph.D., Department of Radiological Sciences, University of California, Peter V. Ueberroth Building, Suite 1471, Room B, 10945 Le Conte Avenue, Los Angeles, CA 90095, USA.
E-mail: daniel.ennis@ucla.edu

Received 15 November 2016; revised 14 March 2017; accepted 16 March 2017

DOI 10.1002/mrm.26705
Published online 00 Month 2017 in Wiley Online Library (wileyonlinelibrary.com).

weighting is characterized by the pulse sequence b-value (b, s/mm^2) and the gradient direction ($\vec{G}$) along which it is applied. This produces a series of images with combined T_2 and diffusion weighting that can be defined by a mono-exponential signal dependence on b and the underlying tissue diffusivity (D, mm^2/ms). In a classical DWI experiment, diffusion-weighted images are normalized by a non-diffusion-weighted acquisition (ie, $b = 0$) in order to extract only the diffusivity from all other sources of contrast. However, considering the T_2 weighting of the spin-echo pulse sequence, the overall signal behavior can be described by a biexponential (Eq. [1])

$$S(b, TE, \vec{G}) = S_0 e^{-TE/T_2} e^{-bD_{\vec{G}}} \quad [1]$$

where S_0 is the non-diffusion- and non-T_2-weighted signal intensity, which is predominantly proton density weighted given a sufficiently long repetition time (TR). $D_{\vec{G}}$ is the diffusivity along the diffusion encoding direction, $\vec{G}$. The resulting estimate of diffusivity from all sampled directions is denoted the ADC. In the proposed T_2+ADC technique, DWI was acquired with multiple TEs and T_2 and ADC were jointly reconstructed using Equation [1].

Because the SNR of cDWI images can be very low (<10), signal averaging is typically used to suppress noise (6,12,13). However, the non-diffusion-weighted reference images ($b = 0$) have significantly higher SNR than those with higher b-values and thus do not require as much signal averaging. Furthermore, whereas conventional DWI uses the same TE for all images to avoid mixing of T_2 and diffusion weighting, a shorter TE is always possible for $b = 0$ attributed to the absence of diffusion-encoding gradients. T_2+ADC leverages the shorter minimum TE when $b = 0$ to improve SNR and enable the estimation of joint T2+ADC maps. By varying the TE of the non-diffusion-weighted images across the repetitions that are necessary to improve SNR for $b > 0$, T_2+ADC mapping can be acquired with no increase in scan time compared with an analogous ADC mapping acquisition with a single, fixed TE.

METHODS

Bloch Simulations

Bloch equation simulations (14) were used to evaluate and optimize the T_2+ADC acquisition for measurement precision and accuracy. The simulations were designed to fulfill two principal objectives: 1) determine the minimum TR necessary for T_2+ADC to be insensitive to T_1 (<1% T_2 bias) and thus to changes in heart rate and 2) determine the optimal distribution of signal averages for each of the TEs to optimize measurement accuracy under the constraint of fixed scan time.

Simulation Parameters

T_2+ADC acquisitions were simulated using a system of 500 independent spins. The signal amplitude during a spin-echo sequence was simulated for two TEs ($TE_1 = 25$ ms; $TE_2 = 65$ ms) and two b-values ($b = 0$ and 350 s/mm^2). TE_1 and TE_2 were the minimum TEs for the desired $2.0 \times 2.0 \times 5.0$ mm spatial resolution with $b = 0$ and 350 s/mm^2, respectively. These specific TEs accorded well with published sampling guidelines for T_2 mapping of the range of expected myocardial T_2 values (15,16). The b-value was chosen to balance SNR, motion insensitivity, and diffusion weighting and was similar to previous cardiac DWI studies (17,18). To incorporate T_2^* effects, the spin system contained a range of off-resonance frequencies ± 50Hz (uniformly distributed, corresponding to $T_2^* \sim$20ms). Repeated simulations were performed over a range of T_1 ($T_1 = 500$, 1,000, and 1,500 ms) and T_2 values ($T_2 = 30$, 40, 50, and 60 ms). The spin ensemble's signal amplitude was measured over a duration surrounding TE corresponding to the duration of the EPI readout ($T_{EPI} = 30$ ms). These signal amplitudes were used to modulate the k-space of a simulated left ventricle (LV) as shown in Figure 1. Diffusion encoding ($D = 1.4$ mm^2/ms, isotropic) was applied to the simulated signals directly using Equation [1] along three directions (x, y, and z). Simulated T_2 and ADC maps were then generated from the resultant signals using Equation [1].

Impact of T_1 on T_2+ADC

To evaluate the impact of T_1 on T_2 and ADC accuracy, the simulation was performed over a range of 10 TRs from 500 to 5,000 ms for every combination of T_1 and T_2 evaluated. Mean T_2 and ADC values were then calculated for each TR within the simulated LV. T_2 and ADC accuracy were evaluated by the percent difference between the mean T_2 and ADC and the predefined input values.

Evaluating Signal Average Distribution

To define the distribution of signal averages for subsequent in vivo acquisitions, complex Gaussian noise was added to the simulated images such that SNR = 50 for $b = 0$ and TE = 25 ms. Scan time was held constant by maintaining the total number of acquired images (10 signal averages per direction for $b = 350$ s/mm^2 and 10 total averages for $b = 0$ and both TE_1 and TE_2). The ratio of averages between TE_1 and TE_2 was, however, varied (ie, $N_{avg,TE1}$:$N_{avg,TE2}$ = 9:1, 8:2, 7:3, etc). Measurement precision was quantified for each acquisition by the standard deviation (SD) of T_2 and ADC values within the simulated LV.

Phantom Experiments

T_2+ADC was acquired in a phantom containing vials of water with varying concentrations of agar and $CuSO_4$, which produced a range of T_1 and T_2 values ($T_1 = 400$–2,000 ms; $T_2 = 30$–150 ms) on a 3 Tesla (T) MRI scanner (Prisma; Siemens, Erlangen, Germany). The T_2+ADC protocol used $TE_1 = 25$ ms and $TE_2 = 65$ ms; TR = 4,000 ms; and $b = 0$ and $b = 350$ s/mm^2 with CODE-M_1M_2 diffusion encoding along three directions (x, y, and z). Three "dummy" cycles (ie, repetitions of the $b = 0$ sequence without readout) were played to ensure the signal reached a steady state before acquiring the first $b = 0$ image. Additional T_2 maps were generated for comparison using: 1) spin-echo imaging with five TEs (TE = 12, 25, 55, 85, and 100 ms; TR = 12 seconds) and 2) T_2-prepared (T_2-prep) balanced steady-state free precession (bSSFP) with three

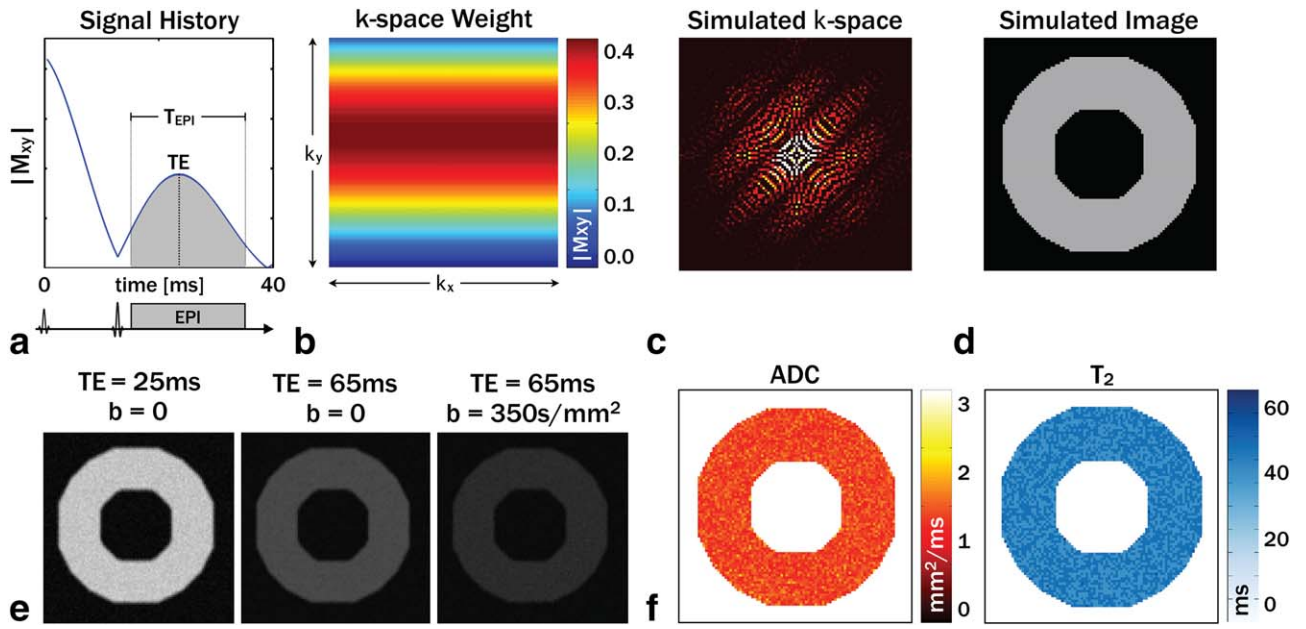

FIG. 1. T_2+ADC Bloch equation simulation framework. (**a**) T_2^* weighting was generated using Bloch equation simulations of the signal during the spin echo acquisition, which generated (**b**) the k-space weighting that modulated line by line the k-space (**c**) corresponding to a simulated LV for two TEs (25 and 65 ms) and two b-values (b = 0 and 350 s/mm^2) (**d**). Complex Gaussian noise was added to the resultant k-space signals to generate noisy images (**e**) that were then used to estimate T_2 and ADC (**f**) according to Equation [1].

T_2-prep durations (t_{prep} = 0, 25, and 55 ms; TR = 3,000 ms), an established technique for myocardial T_2 mapping (19). For comparison, a conventional ADC map was generated using a DWI protocol matched to the T_2+ADC protocol, but with a single TE (TE = 65 ms). Additional protocol details are shown in Table 1.

$T_{2,T2+ADC}$ and $T_{2,bSSFP}$ were compared to the reference $T_{2,SE}$ using regression analysis on mean T_2 values within each of the 10 phantom regions. ADC_{T2+ADC} was similarly compared with the conventional ADC_{DWI}.

Volunteer Experiments

Healthy volunteers (N = 8) were then imaged in an institutional review board–approved study after obtaining written statements of informed consent. Localizers were first acquired to obtain a mid-ventricular short-axis slice that was used for all subsequent imaging. Cine bSSFP images were acquired and visually inspected to determine the timing of the diastolic quiescent period during which bulk cardiac motion was minimized. This subject-specific trigger delay (TD_{DIA}) was used for all subsequent diastolic imaging.

T_2+ADC

Free breathing T_2+ADC images were acquired with respiratory triggering to end-expiration using a liver-dome navigator. Protocol details were: 2.0 × 2.0 × 5.0 mm resolution; field of view (FOV) = 260 × 200 mm; 6/8 partial Fourier (PF), and 2 × parallel imaging acceleration using generalized autocalibrating partially parallel acquisitions (20). Based on simulation results, the non-diffusion-weighted images were acquired with three averages for TE_1 and seven averages for TE_2; b = 350 s/mm^2 images were acquired at TE = 65 ms with 10 averages using CODE-M_1M_2. Imaging was triggered to at least every fourth heartbeat such that TR ≥4,000 ms and three dummy cycles were played before acquiring the first b = 0 image. Inner volume excitation was used to reduce the FOV in the phase encode direction, thereby shortening the readout duration and reducing image distortions (21). TE_2 (b = 0 and 350 s/mm^2) was acquired at mid-systole using TD_{SYS} = 100 ms and at late diastole using TD_{DIA}, whereas TE_1 was shifted (TD_{SYS} + 40 ms and TD_{DIA} + 40 ms) such that imaging occurred at the same cardiac phase (Fig 2). Acquiring 40 images per phase required a total scan time of ~10 minutes.

Image reconstruction was then performed using custom MATLAB code (The Mathworks, Inc., Nattick, MA, USA). Before averaging, all images were coregistered using a rigid transformation to correct for respiratory motion and motion-corrupted voxels were removed using a constrained reconstruction algorithm (22) to correct for

Table 1
Protocol Details for Each of the T_2 and ADC Mapping Sequences

	Resolution [mm]	FOV [mm]	TE [ms]	t_{prep} [ms]	TR [ms]	b [s/mm^2]	Undersampling
T_2+ADC	2.0 × 2.0 × 5.0	260 × 130	25, 65	N/A	4,000	0, 350	6/8 PF, iPAT x2
DWI	2.0 × 2.0 × 5.0	260 × 130	65	N/A	4,000	0, 350	6/8 PF, iPAT x2
bSSFP	1.5 × 1.5 × 5.0	312 × 312	1.17	0, 25, 55	3,000	N/A	6/8 PF
SE	1.0 × 1.0 × 5.0	200 × 200	12, 25, 55, 85, 100	N/A	10,000	N/A	N/A

N/A, not applicable.

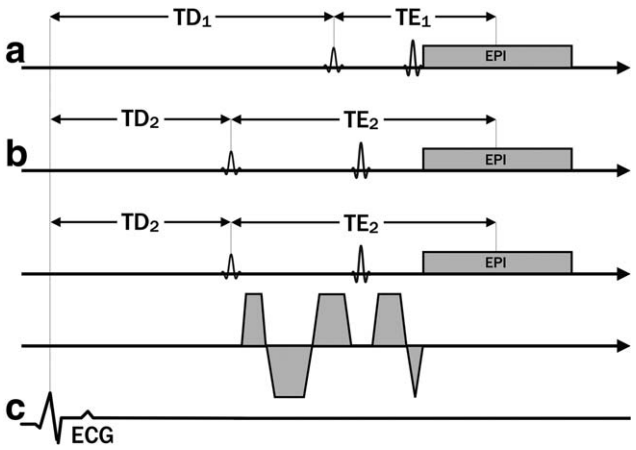

FIG. 2. T_2+ADC pulse sequence diagram. T_2+ADC consists of SE EPI DWI with b = 0 reference images at TE = 25 (**a**) and TE = 65 ms (**b**) to enable T_2 mapping. (**c**) Bulk motion robust CODE-M_1M_2 gradients were used (b = 350 s/mm^2; TE = 65 ms) to obtain cardiac DWI within a reasonable TE. ECG trigger delays were defined for each acquisitions such that imaging always occurred at the same cardiac phase. ECG, electrocardiogram.

artifactual bulk motion signal dropout in the DWI. In this algorithm, a single-gradient direction ADC projection, ADC_0, was calculated for each image, and any voxels in which ADC_0 exceeded 3.0 mm^2/ms (the free diffusivity of water at 37°C, a fundamental limit for diffusion in soft tissue) were discarded.

The T_2+ADC reconstruction was then performed using two methods: 1) a nonlinear fit (NLF) to Equation [1] and 2) a linear fit (LF) to the natural log of Equation [1]. For each fitting method, mean T_2 (μ_{T2}), T_2 SD (σ_{T2}), mean ADC (μ_{ADC}), and ADC SD (σ_{ADC}) were calculated within the LV.

Independent T_2 Mapping

For comparison to T_2+ADC, breath-held T_2-prep bSSFP maps were acquired at the same slice location at mid-systole and diastole in separate breath holds with $1.5 \times 1.5 \times 5.0$ mm resolution, TE = 1.17, TR = 3 heartbeats, linear k-space encoding, and three T_2-prep durations (t_{prep} = 0, 25, and 55 ms). T_2 maps were reconstructed using a least squares linear fit.

Conventional ADC Mapping

ADC maps were also generated from the CODE-M_1M_2 DWI acquired for T_2+ADC, but using only TE = 65 ms at both systole and diastole. ADC values were reconstructed using a least squares linear fit.

T_2 and ADC Map Comparisons

LV masks were manually defined and were used to determine $\mu_{T2,T2+ADC}$, $\sigma_{T2,T2+ADC}$, $\mu_{T2,bSSFP}$, and $\sigma_{T2,bSSFP}$ for each subject at both systole and diastole. μ_{T2} and σ_{T2} reported by each technique were compared using a paired *t* test across the 8 subjects.

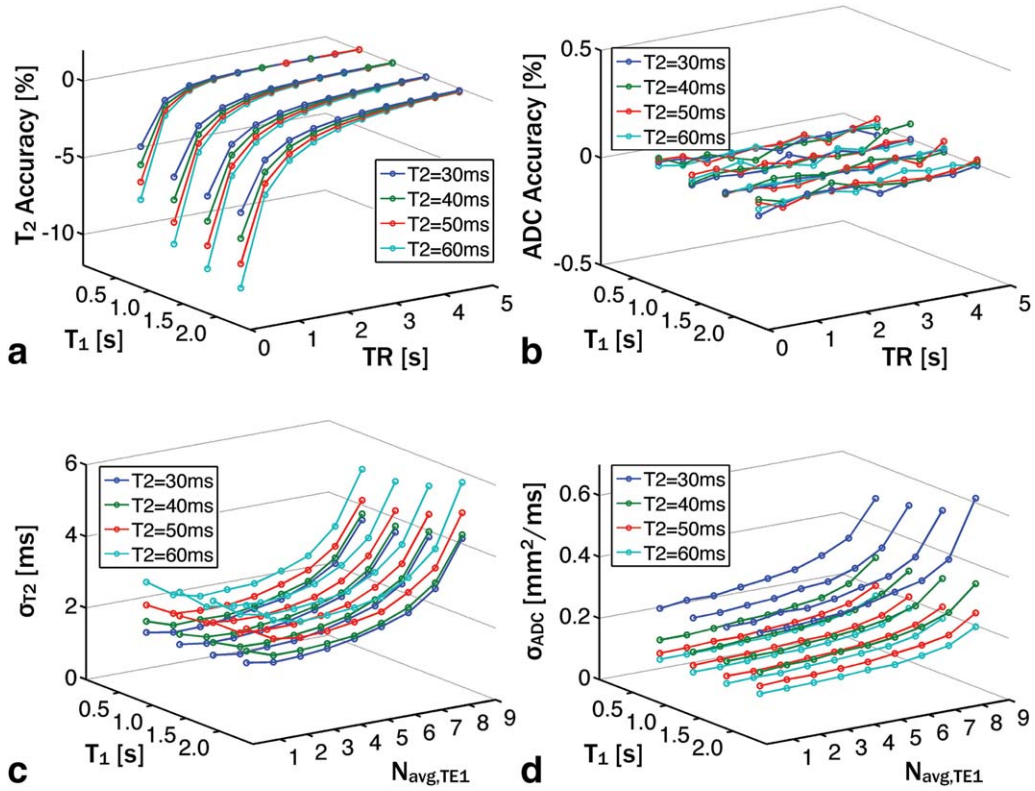

FIG. 3. Bloch simulation results for joint T_2+ADC mapping. T_2 accuracy (**a**) was < 1% when TR ≥ 4000 ms whereas ADC accuracy (**b**) was < 1% for all TRs. T_2 precision (**c**) was minimized when $N_{avg,TE1} = 3$ (TE_1 = 25 ms) and $N_{avg,TE2} = 7$ (TE_2 = 65 ms) for all T_1 ($N_{avg,TE1} + N_{avg,TE2} = 10$). ADC precision (**d**) decreased with decreasing $N_{avg,TE1}$, but the change was negligible with $N_{avg,TE1} \leq 4$.

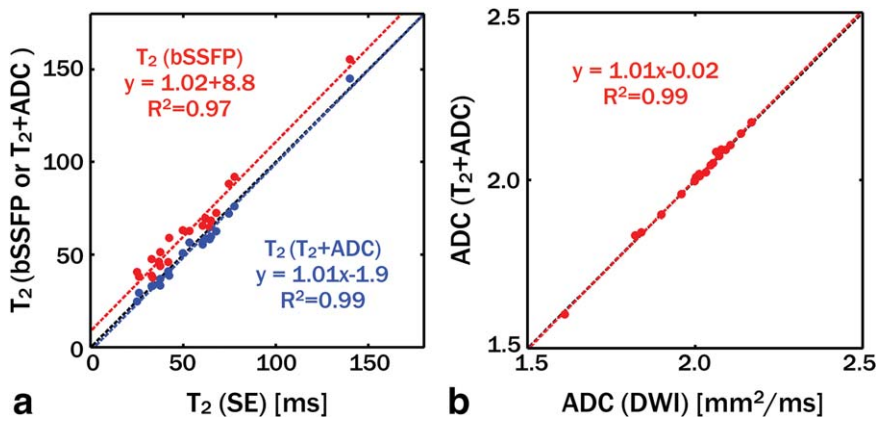

FIG. 4. (**a**) T_2 phantom validation results comparing T_2+ADC (blue) and T_2-prepared bSFFP (red) to conventional SE T_2-mapping. (**b**) compares ADC from T_2+ADC to conventional DWI. Good agreement was observed between T_2 techniques, but bSSFP overestimated T_2 whereas T_2+ADC slightly underestimated T_2 compared with conventional SE. Very high agreement was observed between ADC maps. The dashed black line is the line of unity.

The same analysis was performed on the ADC maps to measure $\mu_{ADC,T2+ADC}$, $\mu_{ADC,DWI}$, $\sigma_{ADC,T2+ADC}$, and $\sigma_{ADC,DWI}$ for each subject at both cardiac phases.

Patient Imaging

T_2+ADC were acquired on a patient undergoing a clinically indicated cardiac MRI examination at 3.0T (Siemens Prisma) with a nonreperfused acute MI in the inferolateral wall, impaired LV ejection fraction (22%), and a pericardial effusion after a failed rescue percutaneous coronary intervention. Imaging parameters were identical to the volunteer experiments, but the acquisition was limited to a single mid-ventricular slice at mid-systole (TD = 100 ms) and the number of averages was reduced to shorten scan time ($N_{avg,TE1} = 2$; $N_{avg,TE2} = 3$; scan time, ~5 minutes). Postcontrast late gadolinium enhanced (LGE) and cine (bSSFP) images were also acquired for reference. Median T_2 and ADC values were measured in manually defined regions of remote and infarcted myocardium as defined on LGE.

RESULTS

Simulations

T_2+ADC Accuracy

T_2+ADC Bloch simulation results are shown in Figure 3. T_2 errors were observed in measurements made with short TRs, but these became negligible (<1%) for all simulated T_1 and T_2 values when TR ≥ 4,000 ms (Fig 3A). For TR = 1,000 ms (approximately one heart beat), T_2 error was as high as 4.6% (for $T_1 = 2{,}000$ ms; $T_2 = 30$ ms). TR had no impact on ADC accuracy (ADC accuracy < 0.1% for all simulated T_1 and T_2 values; Fig 3B).

T_2+ADC Precision

Both T_2 and ADC precision were dependent on the ratio of $N_{avg,TE1}$:$N_{avg,TE2}$ (Fig 3C,D). The precision of both the T_2 and ADC maps was greatest when $N_{avg,TE1}$:$N_{avg,TE2}$ = 9:1. σ_{ADC} decreased monotonically as $N_{avg,TE1}$:$N_{avg,TE2}$ decreased, but with minimal change when $N_{avg,TE1}$: $N_{avg,TE2} \leq 4{:}6$. σ_{T2} was a concave function of $N_{avg,TE1}$ and reached a minimum at $N_{avg,TE1}$:$N_{avg,TE2} = 3{:}7$ for all T_1 values .

Phantom Experiments

Compared with the reference $T_{2,SE}$ maps, T_2+ADC underestimated T_2 ($T_{2,T2+ADC} = 1.01*T_{2,SE} - 1.9$ ms; $R^2 = 0.99$) whereas bSSFP overestimated T_2 ($T_{2,bSSFP} = 1.02*T_{2,SE} + 8.8$ ms; $R^2 = 0.97$) for T_2 values between 30 and 150 ms (Fig 4A). Across all T_2 reference values, $T_{2,T2+ADC}$ was closer to $T_{2,SE}$ and had a lower variance than $T_{2,bSSFP}$ (–2.3 ± 6.0% vs 22.2 ± 16.3%; $P = 2 \times 10^{-7}$). Very high agreement was observed in the diffusion phantom between ADC_{T2+ADC} and conventional ADC_{DWI} ($ADC_{T2+ADC} = 1.01*ADC_{DWI} - 0.02\,mm^2/ms$; $R^2 = 0.99$; mean ADC difference, 0.14 ± 0.39%; Fig 4B).

Volunteer Experiments

Impact of Fitting Algorithm

T_2 and ADC maps were successfully acquired in all 8 volunteers during both systole and diastole using T_2+ADC. The choice of fitting algorithm had no significant impact on the population mean or variance of the T_2 maps (LF-$\mu_{T2} = 37.7 \pm 3.8$ vs NLF-$\mu_{T2} = 37.7 \pm 3.8$ ms; $P = 1.00$; LF-$\sigma_{T2} = 7.4 \pm 1.2$ vs NLF-$\sigma_{T2} = 7.4 \pm 1.2$ ms; $P = 0.99$). NLF and LF mean ADC values were not significantly different (LF-$\mu_{ADC} = 1.58 \pm 0.28$ vs NLF-$\mu_{ADC} = 1.53 \pm 0.25\,mm^2/ms$; $P = 0.56$), but the NLF ADC variance was significantly lower than LF (LF-$\sigma_{ADC} = 0.63 \pm 0.21$ vs NLF-$\sigma_{ADC} = 0.46 \pm 0.15\,mm^2/ms$; $P = 0.01$). With conventional DWI, mean ADC from T_2+ADC mapping was not significantly different from NLF or LF ($\mu_{ADC,DWI} = 1.51 \pm 0.26\,mm^2/ms$; $\mu_{ADC,NLF} = 1.53 \pm 0.25\,mm^2/ms$; $P = 0.48$; $\mu_{ADC,LF} = 1.58 \pm 0.28\,mm^2/ms$; $P = 0.28$). ADC variance from T_2+ADC mapping was significantly lower than LF ($\sigma_{ADC,DWI} = 0.47 \pm 0.15$ vs $\sigma_{ADC,LF} = 0.63 \pm 0.21\,mm^2/ms$; $P = 0.02$), but not different from NLF ($\sigma_{ADC,DWI} = 0.47 \pm 0.15$ vs $\sigma_{ADC,NLF} = 0.46 \pm 0.15\,mm^2/ms$; $P = 0.80$). T_2 and ADC maps generated using both NLF and LF fitting algorithms are shown in Figure 5. All subsequent analysis of

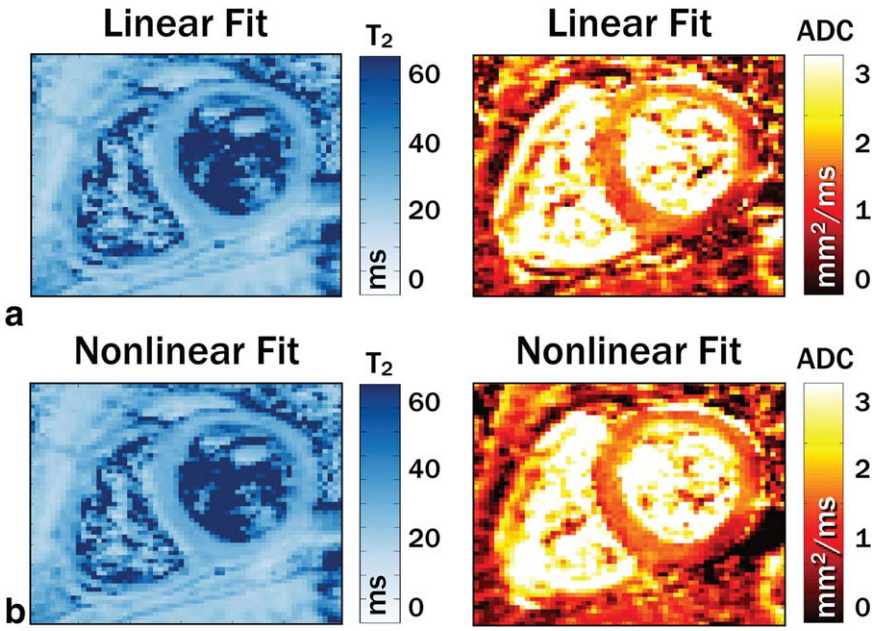

FIG. 5. Example T_2 and ADC maps from T_2+ADC generated using linear fitting (**a**) and nonlinear fitting (**b**). The choice of fitting algorithm had no significant impact on the mean or variance of the T_2 maps. Nonlinear fitting had no significant impact on mean ADC, but led to ADC maps with significantly lower variance ($P = 0.01$).

T_2+ADC was performed using NLF because of the lower NLF ADC variance.

In Vivo T_2 and ADC Mapping

Representative T_2 maps from T_2+ADC and T_2-prep bSSFP at both mid-systole and diastole are shown in Figure 6. ADC maps from T_2+ADC and DWI in the same subject are shown in Figure 7. Mean myocardial T_2 and ADC values (μ_{T2} and μ_{ADC}) as well as myocardial T_2 and ADC variances (σ_{T2} and σ_{ADC}) from each technique are shown in Figures 6 and 7 as well as in Table 2.

Mean myocardial T_2 values from T_2+ADC were significantly lower than bSSFP at both systole and diastole. There were no significant differences in T_2 between systole and diastole within either technique. T_2 variance was significantly lower with T_2+ADC than with T_2-prep bSSFP at both systole and diastole.

There were no significant differences in mean myocardial ADC between T_2+ADC and conventional DWI at either systole or diastole. However, ADC was significantly lower during systole than diastole within both T_2+ADC ($P = 0.02$) and DWI ($P = 0.03$). No significant

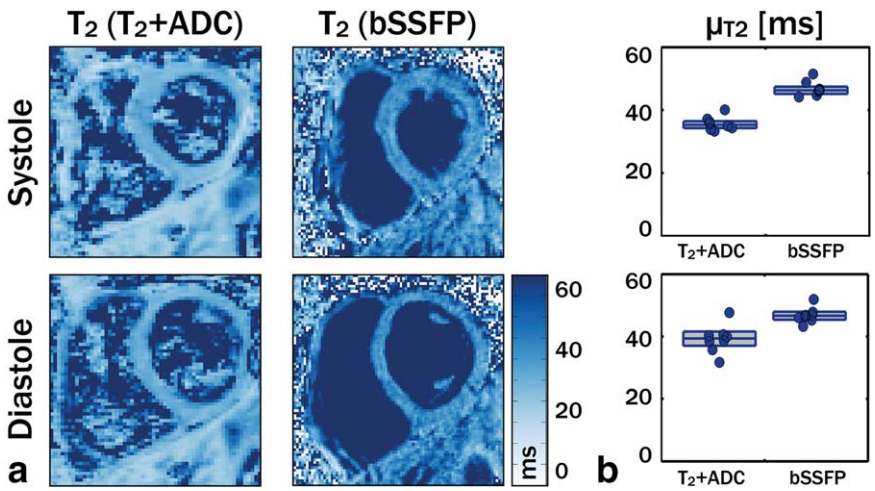

FIG. 6. Representative T_2 maps measured in a healthy volunteer using T_2+ADC and T_2-prepared bSSFP (**a**) at a mid-systolic (top row) and diastolic (bottom row) cardiac phase. The mean myocardial T_2 values (μ_{T2}) measured by each technique for 8 ($N = 8$) subjects are also shown in (**b**). The box edges represent the population mean $\pm$ 1 SD and individual points represent the mean intrasubject value. Consistent with phantom results, T_2+ADC reported significantly lower T_2 values than T_2-prep bSSFP at both systole ($P = 6 \times 10^{-4}$) and diastole ($P = 1 \times 10^{-3}$).

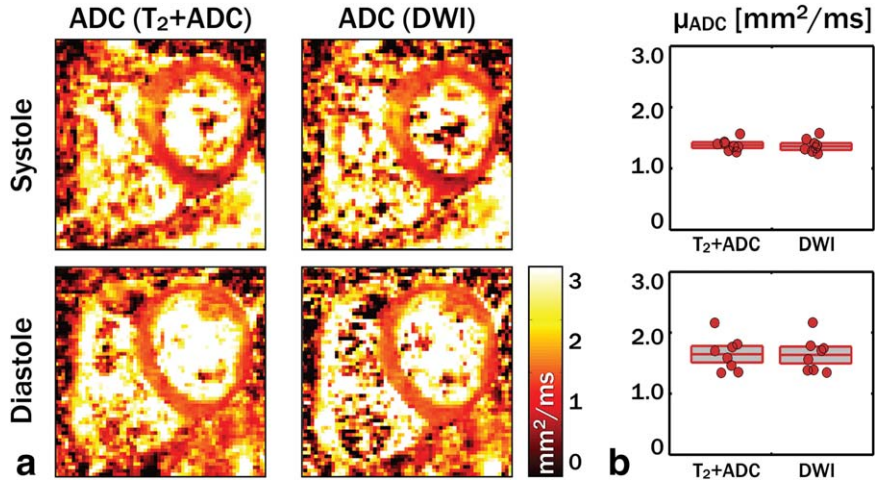

FIG. 7. ADC maps (**a**) from the healthy volunteer shown in Figure 6 using T_2+ADC and DWI at a systolic (top row) and diastolic (bottom row) cardiac phase. The mean myocardial ADC values (μ_{ADC}) measured by each technique for 8 (N = 8) subjects are also shown in (**b**). The box edges represent the population mean ± 1 SD and individual points represent the mean intrasubject value. No significant differences were observed in the ADC values reported by T_2+ADC and DWI at either phase.

differences were observed in ADC variance between T_2+ADC and DWI at systole or diastole.

Patient Imaging

T_2 and ADC maps and histograms from T_2+ADC are shown in Figure 8 along with companion bSSFP and LGE. LGE revealed a large region of enhancement in inferolateral LV free wall. T_2+ADC showed a significant increase in T_2 within the infarct compared with remote myocardium ($T_{2,Remote} = 40.4 \pm 7.6$ vs $T_{2,Infarct} = 56.8 \pm 22.0$ ms; $P < 0.01$) as well as a significant increase in ADC ($ADC_{Remote} = 1.47 \pm 0.59$ vs $ADC_{Infarct} = 1.65 \pm 0.65\,mm^2/ms$; $P < 0.01$).

DISCUSSION

T_2+ADC permitted quantitative estimates of T_2 from cardiac DWI acquisitions with no significant impact on ADC measurement and no increase in scan time compared with conventional DWI. Whereas the simulations indicated that a TR ≥4 seconds (ie, approximately four heart beats) should be used to eliminate T_1 effects, this significantly limits acquisition efficiency. Although a single-slice acquisition was used in this study, T_2+ADC is compatible with multislice imaging approaches (eg, slice following (23)), which would substantially improve acquisition efficiency.

Whereas the linear biexponential fit in T_2+ADC did increase ADC variance compared with conventional DWI, the loss in precision was mitigated by using an NLF in place of the conventional log-linear fit. When using the NLF, there were no significant differences in the mean or variance of myocardial ADC with T_2+ADC compared with DWI. This indicates that T_2+ADC can generate both maps with no cost in scan time compared with DWI and without affecting ADC measurement.

Myocardial T_2 values measured using T_2+ADC were significantly shorter than those reported by bSSFP in both the phantom and in vivo experiments. However, in the phantom, T_2+ADC was closer to the SE reference than bSSFP. This is consistent with reports of bSSFP overestimating T_2, which are likely attributed to T_1 signal weighting (24). It is possible that T_2^* decay during the single-shot SE-EPI readout caused T_2+ADC to underestimate T_2. However, this effect did not bias T_2 measurements in simulations and did not lead to significant errors compared to SE measurements in the phantom study. We expect that the SE sequence produces accurate T_2 measurements because it is free of any stimulated echo effects that are known to lead to errors in multiecho spin-echo T_2 mapping (25–28).

In our experience, the M_1+M_2 nulled diffusion-encoding approach used in this work performs best during systolic imaging because of the consistent and coherent motion during that phase (6,7). Experience shows that diastolic motion tends to be less consistent and varies with changes in heart rate, which can lead to artificially high diastolic ADC values. This was reflected in the higher and more variable ADC values observed in

Table 2
Quantitative In Vivo Results

	Mid-Systole				Diastole			
	μ_{T2} [ms]	σ_{T2} [ms]	μ_{ADC} [mm²/ms]	σ_{ADC} [mm²/ms]	μ_{T2} [ms]	σ_{T2} [ms]	μ_{ADC} [mm²/ms]	σ_{ADC} [mm²/ms]
T_2+ADC	35.8 ± 3.1	6.9 ± 1.1	1.39 ± 0.18	0.41 ± 0.09	39.2 ± 5.4	8.0 ± 1.0	1.64 ± 0.31	0.51 ± 0.18
DWI	N/A		1.38 ± 0.18	0.41 ± 0.08	N/A		1.65 ± 0.32	0.52 ± 0.19
bSSFP	46.8 ± 3.8[a]	12.2 ± 3.2[a]	N/A		46.8 ± 3.4[a]	14.0 ± 4.1[a]	N/A	

[a]Indicates significant differences from T_2+ADC.
N/A, not applicable.

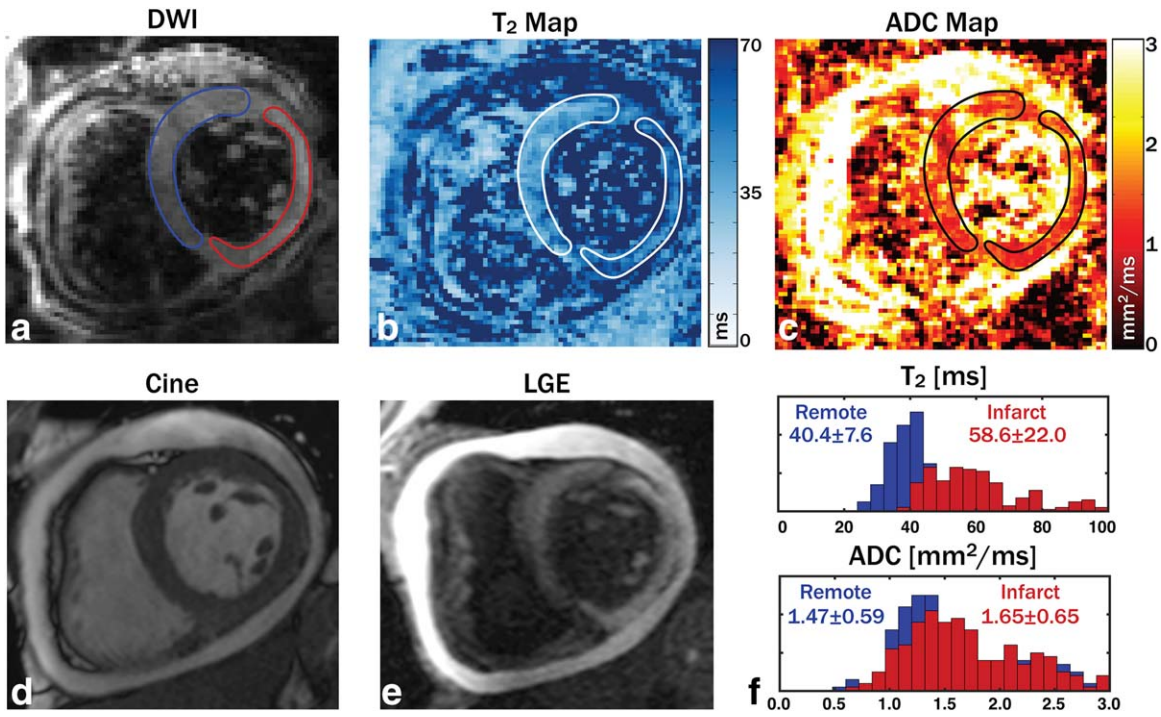

FIG. 8. A representative diffusion weighted image (**a**), T_2 map (**b**), ADC map (**c**), cine image (**d**), and LGE (**e**) from a patient with acute MI. T_2 and ADC were both elevated in the infarct region (lateral wall) compared to the remote myocardium (septal wall; $T_{2,Infarct} = 56.8 \pm 22.0$ vs $T_{2,Remote} = 40.4 \pm 7.6$ ms; $P < 0.01$; $ADC_{Infarct} = 1.65 \pm 0.65$ vs $ADC_{Remote} = 1.47 \pm 0.59\,mm^2/ms$; $P < 0.01$).

diastole with both T_2+ADC and DWI despite the constrained image reconstruction algorithm that eliminates the most severe bulk motion artifacts.

Slightly shorter T_2 values were reported at mid-systole compared to diastole when measured with T_2+ADC, whereas no such decrease was observed in bSSFP. This difference could also be caused by bulk motion sensitivity in the SE-EPI pulse sequence. The second-order moment of the crusher gradients surrounding the refocusing pulse used for the $b = 0$ acquisitions depends on their timing within the pulse sequence (29). Consequently, acquisitions with long TEs are more bulk-motion sensitive than those with short TEs. This could lead to additional signal decay for longer TEs, which would shorten the apparent T_2 from T_2+ADC, as observed in mid-systole compared with diastole. Furthermore, inconsistent motion during of diastole may have led to the increase in T_2 variability in diastole.

One drawback of T_2 mapping with T_2+ADC compared with T_2-prep bSSFP is the impact of single-shot SE EPI on image quality, which has known issues with distortion and chemical shift in the heart (30). The use of inner volume excitation combined with high-performance imaging gradients significantly mitigates these issues by shortening the EPI readout, but further work is necessary to improve image quality. Furthermore, the minimum TE achievable in T_2+ADC is directly linked to the EPI readout duration, which, in turn, limits spatial resolution for a given TE. Parallel imaging and PF were used to shorten the EPI readout and thereby decrease the minimum achievable TE and mitigate EPI distortions. However, this impacts SNR, which necessitated signal averaging. In the present study, the minimum TE of 25 ms appeared to be sufficiently short for healthy myocardial T_2 quantification, but this may present a problem with shortened T_2 values in conditions such as thalassemia (31). These drawbacks could potentially be avoided by adapting T_2+ADC to a diffusion prepared acquisition (5) at the cost of a significantly longer temporal footprint attributed to the duration of a single or multishot bSSSP readout compared with single-shot EPI.

The preliminary T_2+ADC mapping results in acute MI indicate that this technique is applicable in severely ill patients and can detect the presence of fibrosis and edema. Notably, there was good agreement between ADC values in remote myocardium for this patient and those measured in volunteers. Remote T_2 values were slightly longer than what was observed in volunteers at mid-systole, which indicates the presence of global inflammation which is expected after acute MI (32). Infarct T_2 values were consistent with those reported by Giri et al (9), but infarct ADC values were lower than values observed by Nguyen et al (18).

CONCLUSION

T_2+ADC is a novel technique for simultaneously estimating T_2 and ADC in the heart during a free-breathing acquisition. T_2+ADC generated perfectly coregistered maps and had no impact on ADC accuracy, ADC precision, or scan time compared with conventional DWI while making precise measurements of myocardial T_2.

ACKNOWLEDGMENTS

The authors thank Drs Pierre Croisille and Magalie Viallon for the clinical data set presented in this work.

REFERENCES

1. Wehrli FW, Saha PK, Gomberg BR, Song HK, Snyder PJ, Benito M, Wright A, Weening R. Role of magnetic resonance for assessing structure and function of trabecular bone. Top Magn Reson Imaging 2002; 13:335–355.
2. Nguyen C, Fan Z, Xie Y, Dawkins J, Tseliou E, Bi X, Sharif B, Dharmakumar R, Marban E, Li D. In vivo contrast free chronic myocardial infarction characterization using diffusion-weighted cardiovascular magnetic resonance. J Cardiovasc Magn Reson 2014;16:68.
3. Perazella MA, Rodby RA. Gadolinium-induced nephrogenic systemic fibrosis in patients with kidney disease. Am J Med 2007;120:561–562.
4. Saran R, Li Y, Robinson B, et al. US Renal Data System 2014 Annual Data Report: Epidemiology of Kidney Disease in the United States. Am J Kidney Dis 2015;65(6 Suppl 1):A7.
5. Nguyen C, Fan Z, Sharif B, He Y, Dharmakumar R, Berman DS, Li D. In vivo three-dimensional high resolution cardiac diffusion-weighted MRI: a motion compensated diffusion-prepared balanced steady-state free precession approach. Magn Reson Med 2013;72:1257–1267.
6. Stoeck CT, von Deuster C, Genet M, Atkinson D, Kozerke S. Second-order motion-compensated spin echo diffusion tensor imaging of the human heart. Magn Reson Med 2016;75:1669–1676.
7. Aliotta E, Wu HH, Ennis DB. Convex optimized diffusion encoding (CODE) gradient waveforms for minimum echo time and bulk motion compensated diffusion weighted MRI. Magn Reson Med 2017;77:717–729.
8. Higgins CB, Herfkens R, Lipton MJ, Sievers R, Sheldon P, Kaufman L, Crooks LE. Nuclear magnetic resonance imaging of acute myocardial infarction in dogs: alterations in magnetic relaxation times. Am J Cardiol 1983;52:184–188.
9. Giri S, Chung YC, Merchant A, Mihai G, Rajagopalan S, Raman SV, Simonetti OP. T2 quantification for improved detection of myocardial edema. J Cardiovasc Magn Reson 2009;11:56.
10. Guo H, Au WY, Cheung JS, Kim D, Jensen JH, Khong PL, et al. Myocardial T2 quantitation in patients with iron overload at 3 Tesla. J Magn Reson Imaging 2009;30:394–400.
11. Kali A, Cokic I, Kumar A, Tsaftaris S, Tang RL, Friedrich MG, Dharmakumar R. Acute reperfusion intramyocardial hemorrhage leads to regional chronic iron deposition in the heart. J Cardiovasc Magn Reson 2013;15(Suppl 1):P174.
12. Nielles-Vallespin S, Mekkaoui C, Gatehouse P, Reese TG, Keegan J, Ferreira PF, et al. In vivo diffusion tensor MRI of the human heart: reproducibility of breath-hold and navigator-based approaches. Magn Reson Med 2013;70:454–465.
13. McGill LA, Scott AD, Ferreira PF, et al. Heterogeneity of fractional anisotropy and mean diffusivity measurements by in vivo diffusion tensor imaging in normal human hearts. PLoS One 2015;10:e0132360.
14. Hargreaves BA. Bloch Equation Simulator. 2002. Available at: http://mrsrl.stanford.edu/~brian/mritools.html. Accessed October 1, 2016.
15. Fleysher L, Fleysher R, Liu S, Zaaraoui W, Gonen O. Optimizing the precision-per-unit-time of quantitative MR metrics: examples for T1, T2, and DTI. Magn Reson Med 2007;57:380–387. Accessed October 1, 2016.
16. Zhang Z, Aliotta E, Ennis D. Optimized acquisition for joint T2 and ADC mapping in the Heart. In Proceedings of the 24th Annual Meeting & Exhibition of ISMRM, Singapore, 2016. Abstract 3159.
17. Gamper U, Boesiger P, Kozerke S. Diffusion imaging of the in vivo heart using spin echoes--considerations on bulk motion sensitivity. Magn Reson Med 2007;57:331–337.
18. Nguyen C, Lu M, Fan Z, Bi X, Kellman P, Zhao S, Li D. Contrast-free detection of myocardial fibrosis in hypertrophic cardiomyopathy patients with diffusion-weighted cardiovascular magnetic resonance. J Cardiovasc Magn Reson 2015;17:107.
19. Huang TY, Liu YJ, Stemmer A, Poncelet BP. T2 measurement of the human myocardium using a T2-prepared transient-state TrueFISP sequence. Magn Reson Med 2007;57:960–966.
20. Griswold MA, Jakob PM, Heidemann RM, Nittka M, Jellus V, Wang J, Kiefer B, Haase A. Generalized autocalibrating partially parallel acquisitions (GRAPPA). Magn Reson Med 2002;47:1202–1210.
21. Feinberg DA, Hoenninger JC, Crooks LE, Kaufman L, Watts JC, Arakawa M. Inner volume MR imaging: technical concepts and their application. Radiology 1985;156:743–747.
22. Aliotta E, Rapacchi S, Hu P, Ennis D. Increased maximum gradient amplitude improves robustness of spin-echo cardiac diffusion-weighted MRI. In Proceedings of the 18th Annual SCMR Scientific Sessions, France, 2015. p. 4–7.
23. Moulin K, Croisille P, Feiweier T, Delattre BM, Wei H, Robert B, Beuf O, Viallon M. In vivo free-breathing DTI and IVIM of the whole human heart using a real-time slice-followed SE-EPI navigator-based sequence: a reproducibility study in healthy volunteers. Magn Reson Med 2016;76:70–82.
24. Salerno M, Kramer CM. Advances in parametric mapping with CMR imaging. JACC Cardiovasc Imaging 2013;6:806–822.
25. Majumdar S, Orphanoudakis SC, Gmitro A, O'Donnell M, Gore JC. Errors in the measurements of T2 using multiple-echo MRI techniques. II. Effects of static field inhomogeneity. Magn Reson Med 1986; 3:562–574.
26. Majumdar S, Orphanoudakis SC, Gmitro A, O'Donnell M, Gore JC. Errors in the measurements of T2 using multiple-echo MRI techniques. I. Effects of radiofrequency pulse imperfections. Magn Reson Med 1986;3:397–417.
27. Crawley AP, Henkelman RM. Errors in T2 estimation using multislice multiple-echo imaging. Magn Reson Med 1987;4:34–47.
28. Sussman MS, Vidarsson L, Pauly JM, Cheng HL. A technique for rapid single-echo spin-echo T2 mapping. Magn Reson Med 2010;64: 536–545.
29. Bernstein MA, King KF, Zhou ZJ. Handbook of MRI pulse sequences. Amsterdam; Boston, MA: Academic; 2004, 320 p.
30. Ferreira PF, Gatehouse PD, Mohiaddin RH, Firmin DN. Cardiovascular magnetic resonance artefacts. J Cardiovasc Magn Reson 2013;15: 41.
31. He T, Gatehouse PD, Anderson LJ, Tanner M, Keegan J, Pennell DJ, Firmin DN. Development of a novel optimized breathhold technique for myocardial T2 measurement in thalassemia. J Magn Reson Imaging 2006;24:580–585.
32. Manrique A, Gerbaud E, Derumeaux G, Cribier A, Bertrand D, Lebon A, Dacher JN. Cardiac magnetic resonance demonstrates myocardial oedema in remote tissue early after reperfused myocardial infarction. Arch Cardiovasc Dis 2009;102:633–639.